Article

Post-Flood UAV-Based Free Space Optics Recovery Communications with Spatial Mode Diversity

Angela Amphawan [1,2,*], **Norhana Arsad** [3], **Tse-Kian Neo** [4], **Muhammed Basheer Jasser** [1,2] **and Athirah Mohd Ramly** [1,2]

1   Photonics Laboratory, School of Engineering and Technology, Sunway University, Petaling Jaya 47500, Selangor, Malaysia; basheerj@sunway.edu.my (M.B.J.); athirahr@sunway.edu.my (A.M.R.)
2   Elasticities Research Cluster, Sunway University, Petaling Jaya 47500, Selangor, Malaysia
3   Faculty of Engineering & Built Environment, Universiti Kebangsaan Malaysia, Bangi 43600, Selangor, Malaysia; noa@ukm.edu.my
4   Institute for Digital Education and Learning, Multimedia University, Cyberjaya 63100, Selangor, Malaysia; tkneo@mmu.edu.my
*   Correspondence: angelaa@sunway.edu.my

Abstract: The deployment of unmanned aerial vehicles (UAVs) for free space optical communications is an attractive solution for forwarding the vital health information of victims from a flood-stricken area to neighboring ground base stations during rescue operations. A critical challenge to this is maintaining an acceptable signal quality between the ground base station and UAV-based free space optics relay. This is largely unattainable due to rapid UAV propeller and body movements, which result in fluctuations in the beam alignment and frequent link failures. To address this issue, linearly polarized Laguerre–Gaussian modes were leveraged for spatial mode diversity to prevent link failures over a 400 m link. Spatial mode diversity successfully improved the bit error rate by 38% to 55%. This was due to a 10% to 19% increase in the predominant mode power from spatial mode diversity. The time-varying channel matrix indicated the presence of nonlinear deterministic chaos. This opens up new possibilities for research on state-space reconstruction of the channel matrix.

Keywords: free-space optical communication; spatial mode diversity; unmanned aerial vehicle; emergency recovery communications; floods

1. Introduction

The risk of floods is rising worldwide, due to an increase in the intensity and frequency of rainfalls as a consequence of global warming [1]. Floods cause fatalities, damage to buildings, deterioration of health conditions, severe economic losses, losses of livelihood, and disruption of global trade [2]. Globally, it is estimated that floods have directly affected 2.3 billion people and caused USD 662 billion in damages between 1995 and 2015 [3]. In Malaysia, destructive floods occur frequently in the three eastern states of the peninsular during the seasonal monsoon between October and March, affecting more than 4.8 million people annually [4]. In the recent December 2021 massive nationwide flood, as many as eight states were struck by a 1-in-a-100-year heavy rainfall spanning two weeks, which displaced thousands of residents and strained emergency services [5–7]. The aftermath of the floods also witnessed unscheduled water cuts and disruptions to the electricity supply [8,9]. In addition, telecommunication base stations were severely damaged, leading to the disruption of communication services [10,11]. This prevented the exchange of situational awareness and hampered the coordination of search and rescue operations.

To connect emergency responders to flood rescue centers and to victims, several recovery communications technologies are being explored, as shown in Figure 1. To compensate for flood-impaired ground radio base stations, satellites have been considered due its large

capacity and wide coverage. This requires the design of satellite constellations comprising multiple satellites across several countries for reliable coverage in the flood-stricken area, and to backhaul unflooded cells via satellite [12–14]. High-altitude platforms (HAPs) such as airships, aerostats, and balloons have been used to ferry antennas in the affected area, for relaying data to neighboring ground base stations to a large number of users [15]. HAPs are located in the stratosphere, enabling a wide coverage and accommodating a large number of users [16]. Compared to satellites, HAPs provide a higher area throughput and resource utilization [15]. HAPs can also distribute the recording of the orbital paths of satellites and monitor the probability of a collision between satellites [17]. Data transmission from a HAP involves the control of the HAP flight trajectory and the transmit power of the HAP antenna [18–20].
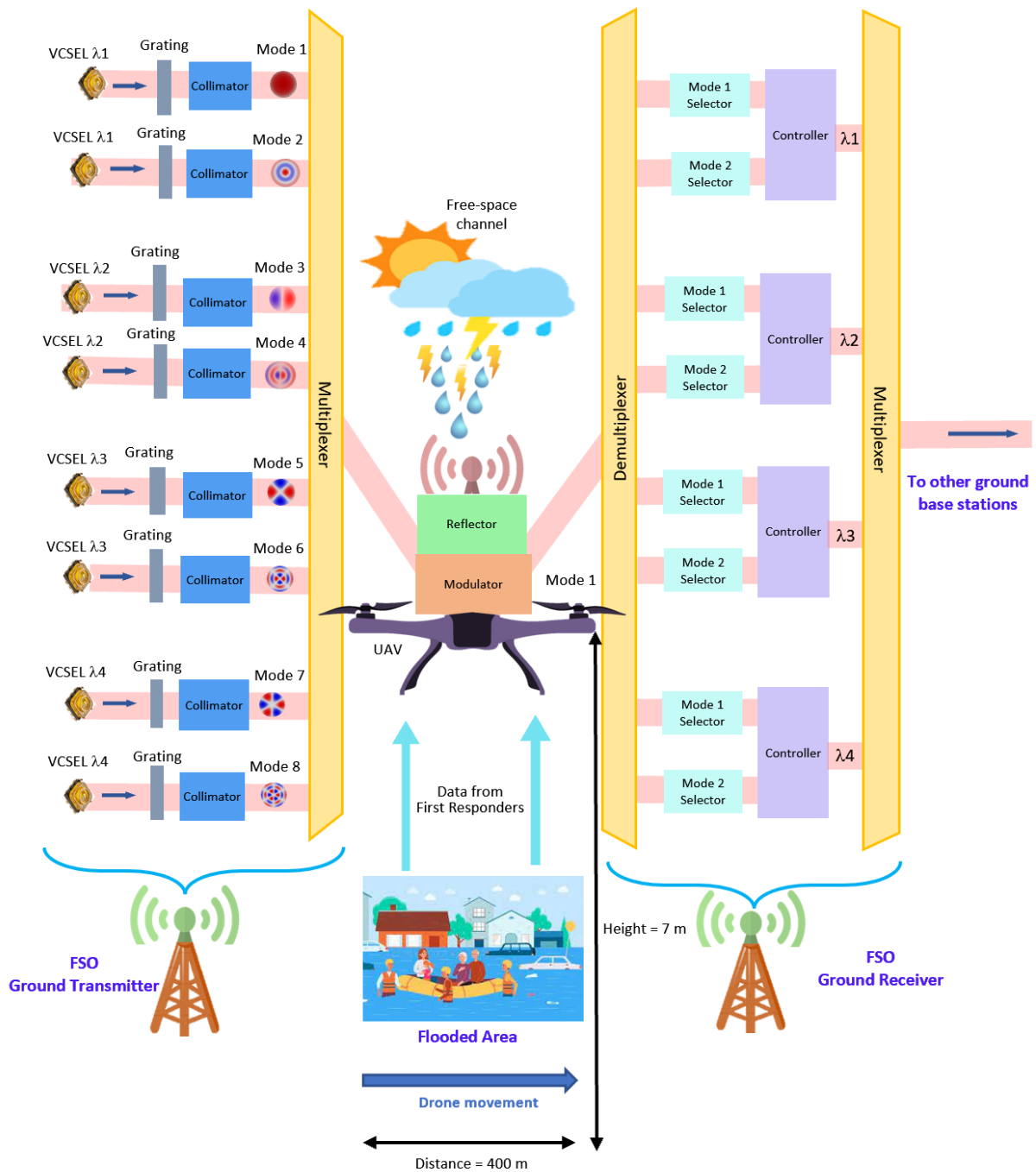

Figure 1. UAV-based spatial mode diversity free space optics (FSO) system for post-flood recovery communications.

Recently, the deployment of unmanned aerial vehicles (UAVs) during natural disasters has become increasingly prevalent for forwarding information from the affected area to undamaged ground base stations during rescue operations [21]. UAVs generally have limited onboard energy [22]. Typically, several UAVs are connected in topologies such as a mesh, star, or cluster. UAVs are linked to each other in order to reach the undamaged ground base station, in conjunction with routing and positioning algorithms [23–26].

The remainder of the paper organized as follows. Section 2 provides an overview of free space optics (FSO) for post-flood recovery communications and related work on spatial mode diversity using FSO. Section 3 elucidates the novelty and contributions of the paper. Section 4 describes the design of a UAV-based spatial mode diversity FSO system for post-flood recovery communications. Section 5 reports on the performance analysis of the proposed system.

2. Free Space Optics for Post-Flood Recovery Communications

Free space optics is an attractive solution during floods when conventional base stations spanning several cities have been damaged, providing connectivity to the flood-stricken area and ensuring minimal disruption in unaffected areas. Free space optics provides a high data bandwidth and rapid deployment, without spectrum licensing costs [27,28]. In addition, the light signals can penetrate easily through water droplets [29].

Although satellites and HAPs cover a larger area, the deployment time is longer [30]. Motivated by the rapid deployment and agility of UAVs for recovery communications [22,30], a UAV-based FSO is proposed as a wireless access technology for rapid recovery communications during floods.

Several UAV-based FSO strategies have previously been developed for recovery communications between base stations for recovery communications, focusing on downlink scheduling [31], and the placement of FSO transceivers [32,33], divergence angle [34], or hybrid radio frequency (RF)/FSO links [35,36]. An unveiled challenge to UAV-based FSO systems is to maintain a high SNR between the base station and UAV-based FSO relay. This is largely unattainable due to minute but rapid UAV propeller and body movements, which result in swift fluctuations in the beam alignment and water scattering from flood waters. Consequently, this would lead to frequent link failures. To address this issue, spatial mode diversity is proposed for improving the resilience of the system from UAV movements.

Harnessing spatial modes as independent information carriers using space division multiplexing (SDM) techniques has recently gained traction for tackling the impending data capacity crunch [37]. Spatial modes provide an additional degree of freedom in wireless communications. Characteristically, in a SDM system, independent data-carrying beams are structured on distinct spatial modes that can be multiplexed at the transmitter aperture for co-transmission and demultiplexed at the receiver aperture, with minimal interference [37].

To increase the resilience of an FSO system, multiplexing in the amplitude, frequency, polarization, and time domains have been employed. Recently, a new degree of freedom based on spatial modes is being explored. The simultaneous transmission of several spatial modes can be realized without the separation between apertures, thus reducing the device footprint. Individual spatial modes encounter different refractive index perturbations from atmospheric turbulence, despite propagating in the same path [38,39]. Spatial modes may be leveraged for transmission of independent data streams to improve link reliability and prevent network interruption.

Several approaches have been demonstrated for spatial mode diversity in FSO systems. In [40], spatial mode diversity was employed in conjunction with multiple transmitter-receiver aperture pairs to improve FSO link reliability under atmospheric turbulence. Three aperture pairs were used and each aperture pair utilized a Gaussian beam and an OAM beam in the uplink and downlink direction simultaneously for carrying the same data stream. In [41], spatial mode diversity from a three-mode photonic lantern coupling FSO receiver was designed in conjunction with a digital maximal ratio combining

to enhance the worst signal-to-noise ratio (SNR) by more than 10 dB and to mitigate the interruption probability under atmospheric turbulence. In [42], the three-mode diversity reception in free space optical links from low-Earth orbital satellites to a ground terminal was demonstrated by mode coupling to a few-mode fiber for tracking power variations under different elevation angles. In [43], to reduce the outage probability, aperture diversity was realized through several transmitter apertures transmitting the same data stream on fundamental Gaussian beams whilst mode diversity was realized through multiple receiver apertures that decompose the incoming beam to several orbital angular momentum (OAM) modes, in conjunction with digital signal processing. In [44], OAM modes were used for spatial mode diversity through a 2 km FSO link to improve the link resilience and system capacity. The overall channel capacity was maximized by selecting optimal OAM mode numbers at each value of the SNR and turbulence strength. Spatial mode diversity has also been demonstrated using photonic crystal fibers [45–48]. Another approach for spatial mode diversity was demonstrated using Hermite-Gaussian (HG) and Laguerre-Gaussian (LG) modes of identical size [39]. This was shown to improve the bit error rate by up to 54% without an increase in the total transmit power or radius of the receive aperture. Unmanned aerial vehicle (UAV)-based FSO strategies have been explored for improving coverage between base stations for emergency communications during natural disasters, focusing on downlink scheduling [31] and the placement of FSO transceivers [32,33] and hybrid RF/FSO links [35,36].

3. Contributions

The disastrous aftermath of floods has reinforced the need for complementary access networks for critical recovery communications from the flood-stricken area to unaffected areas [21]. In the event where many conventional base stations spanning several cities are damaged, unlicensed, high-bandwidth wireless access technology is required for complementary post-flood recovery communications, to expedite communications to the flood-stricken area. Connecting first responders and healthcare workers to flood victims and hospitals is an integral part of recovery communications. Several UAV-based FSO strategies have previously been developed for recovery communications between base stations for recovery communications, focusing on downlink scheduling [31], the placement of FSO transceivers [32,33], divergence angle [34], or hybrid RF/FSO links [35,36]. An unveiled challenge to UAV-based FSO systems is to maintain a high SNR between the base station and UAV-based FSO relay. This is largely unattainable due to minute but rapid UAV propeller and body movements, which result in swift fluctuations in the beam alignment and water scattering from flood waters. Consequently, this would lead to frequent link failures. To address this issue, spatial mode diversity is proposed using linearly polarized modes for improving the resilience of the system from UAV movements.

4. Methods

The proposed UAV-based spatial mode diversity FSO system for post-flood recovery communications is illustrated in Figure 1. Four vertical cavity surface-emitting lasers (VCSELs) generating continuous-wave optical signals on the fundamental modes at wavelengths of 850 nm, 880 nm, 910 nm, and 940 nm were structured into eight distinct linearly polarized Laguerre–Gaussian beams, *LP lm*, where *l* = 0, 1, 2, 3, 4 and *m* = 1, 3. The LG beams were intensity-modulated at 20 Gbps by pre-processed binary data collected from individual sensors on their respective channels. The *LP* modes and wavelengths used for the respective channels are shown in Table 1. The ground transmitter was enclosed in a case for protection from rain.

Table 1. Channel Characteristics.

Channel/Mode, i	Mode, LP lm	Signal	Type	Wavelength
1	LP 01	Sensor 1	Primary	850 nm
2	LP 03	Sensor 1	Backup	850 nm
3	LP 11	Sensor 2	Primary	880 nm
4	LP 13	Sensor 2	Backup	880 nm
5	LP 21	Sensor 3	Primary	910 nm
6	LP 23	Sensor 3	Backup	910 nm
7	LP 31	Sensor 4	Primary	940 nm
8	LP 33	Sensor 4	Backup	940 nm

LP lm modes were generated from the first diffraction order in the Fourier plane using the binarized electric field displayed on individual liquid crystal gratings, as follows. It is known that the Fourier transform of a linear translation is a complex phase shift [49]. Thus, to produce a translation in the Fourier plane, the transverse modal field is first multiplied by a complex phase shift:

$$\exp[j(\tau_x x + \tau_y y)] \tag{1}$$

where τ_x and τ_y are linear tilt constants in the horizontal and vertical directions, respectively.

The complex tilted field of the *LP* mode, $a + jb$, is binarized such that, in regions represented by

$$\left(b \pm \frac{1}{2}\right)^2 + a^2 \geq \frac{1}{4}, \quad a \leq 0 \tag{2}$$

an expanded laser beam is transmitted through a liquid crystal display, and in other regions, no light passes through. The binarized beam may be expressed as a Fourier series expansion [45–48,50]:

$$g(x_1, y_1) = m_o + \frac{4}{\pi} \sum_{n=1}^{\infty} m_n \, \cos\left\{n\left[\xi(x_1, y_1) + \tau_x x_1 + \tau_y y_1\right]\right\} \tag{3}$$

where m_o is the constant term and n is the *n-th* diffraction order. In the Fourier plane, the diffraction orders are translated linearly and separated:

$$G(x_2, y_2) = M_o(x_2, y_2) \, + \, \sum_{n=1}^{\infty} \left[M_n(x_2 + n\tau_x, \, y_2 + n\tau_y) + M_n^*(n\tau_x - x_2, n\tau_y - y_2)\right] \tag{4}$$

where x_2 and y_2 are spatial coordinates in the Fourier plane, * is the complex conjugate, and $M_n(x_2, y_2)$ is the *n*-th diffraction order in the Fourier plane.

Each binarized field was then Fourier transformed by a 400 cm focal-length achromatic convex lens, and the linearly polarized Laguerre–Gaussian mode, *LP lm*, was extracted from the first diffraction order in the Fourier plane, M1.

The transverse modal field distribution of a linearly polarized *LP lm* mode is expressed as [51]:

$$E = R^l L_{m-1}^l(VR^2) \exp\left(-VR^2/2\right) \cos\phi \tag{5}$$

where R is the normalized radius, ϕ is the azimuthal angle of the transmitted transverse modal field, V is the normalized frequency, L_{m-1}^l is the generalized Laguerre polynomial whereby l is the azimuthal mode number, and m is the radial mode number.

For channel diversity, each sensor transmitted data on two *LP* modes so that they experience distinct refractive index fluctuations and modal power coupling. For any data stream, the first mode was used as the primary channel, and a second mode was used as the backup channel during adverse weather conditions, such as rain. Different combinations of the azimuthal mode number and radial mode numbers were used for various primary and backup channels, as shown in Table 1. The backup channels operated on different *LP*

modes from the primary channels, thus experiencing distinct refractive index fluctuations and mode coupling.

The optical signals from all channels were then amplified, multiplexed, aligned, and transmitted to the UAV, which was flown at a height of 7 m above ground, in a straight line toward the ground receiver, located 40 m away from the transmitter. The horizontal distance travelled and height of the flying drone is shown in Figure 1. Following this, the optical beams are reflected from the UAV to the ground receiver. System parameters are provided in Table 2. The beam waist is the location along the propagation direction where the beam radius is minimum. The Rayleigh length is the distance from the beam waist, in the direction of beam propagation, where the beam radius is increased by a factor of the square root of 2. The beam divergence is an angular measure of the increase in beam diameter or radius with distance from the grating. The photodetector responsivity is a measure of optical-to-electrical conversion efficiency of a photodetector.

Table 2. Systems Parameters.

Parameter	Value
Beam waist	0.025 m
Operating wavelengths	850 nm, 880 nm, 910 nm and 940 nm
Rayleigh range	0.5 m
Propagation distance	400 m
Transmitted beam diameter	3 mm
Beam divergence	0.5 mrad
Photodetector responsivity	0.6 A/W
Focal lengths of transmitter lens	40 cm

The transverse electric field of the set of eight *LP* modes used for the transmission may be modeled as:

$$X = [X_1 \ X_2 \ X_3 \ldots \ X_8]^T \tag{6}$$

where X_i is the transverse electric field of the transmitted i-th mode and T is the transpose of the matrix. The estimated received electric field after propagating through the FSO channel is

$$Y = [Y_1 \ Y_2 \ Y_3 \ldots \ Y_8]^T, \tag{7}$$

where Y_i is estimated electric field of the i-th received mode and T is the transpose of the matrix. Y is related to the channel matrix, H by [52]

$$Y = HX + N, \tag{8}$$

where the channel matrix H contains the power coupling coefficients,

$$h_{i,j}, \quad i,j \in [1, N] \tag{9}$$

A charge-coupled device was used to collect the intensity distribution of the received optical signals. The power coupling coefficients were computed for all channels using a modal decomposition method [53].

Multiplicative slow fading and inter-symbol interference from adjacent modes $i \neq j$ were assumed. N is additive noise from the surroundings.

The received electric field of the i-th mode may be estimated as the summation of the individual components of the transmitted electric field, X_j [54]:

$$Y_i = \sum_j h_{i,j} X_j + N \tag{10}$$

The power coupling coefficient $h_{i,j}$ is the overlap integral between the received transverse electric field, Y_i, and transmitted transverse electric field, X_j [55]:

$$h_{i,j} = \frac{\left| \int\limits_A Y_i(x,y) \cdot X_j^*(x,y)\, dA \right|^2}{\int\limits_A |Y_i(x,y)|^2 dA \; \int\limits_A |X_j(x,y)|^2 dA} \tag{11}$$

where A is the plane of the transverse electric field. When the set of modes propagate through the atmosphere, it encounters spatially and temporally varying refractive indices, due to random pressure temperature variations. Spatial modes individually experience different refractive index perturbations, even when propagating in the same path [39]. This causes unique random wavefront aberrations and power spreading for each mode into adjacent modes, evident by the degradation of power coupled into the original mode $h_{i,j}$. Under atmospheric turbulence, these power fluctuations are slowly time-varying and vary significantly slower than the signal [56,57].

The Kolmogorov model for turbulent flow is the basis for many contemporary theories and models for emulating atmospheric turbulence for spatial modes [52,58–60]. However, these models of turbulence typically only provide statistical averages for the random variations of the atmosphere. Thus, they may be considered insufficient to represent temporal intensity fluctuations and modal crosstalk for a UAV-based system. Hence, in our work, in order to demonstrate the performance of mode diversity for maintaining the signal quality for composite channels, the time-varying optical signal-to-interference-and-noise ratio (SINR) was evaluated under various weather conditions over a time interval of 30 min and sampling interval of 1 s. The optical SINR for the i-th channel is given by:

$$\begin{aligned} SINR_i &= \frac{P_i}{I_i + N} \\ &= \frac{\left| h_{i,\,j=i} \right|^2}{\left| h_{i,\,j \neq i} \right|^2 + N} \end{aligned} \tag{12}$$

where P_i is the received power from the i-th desired mode ($j = i$), either in the primary channel or the backup channel. The measured interference power I_i arises from crosstalk from undesirable spatial modes ($j \neq i$). The measured additive noise power, N, constituting thermal noise, ambient light from sunlight, and surrounding objects is minimal compared to the interfering modal power.

For optimal signal detection, the ground receiver requires knowledge of the current channel matrix, H. The main challenge lies in the alignment between the ground transmitter to the UAV and the alignment between the UAV to the ground receiver, in order to prevent tip-tilt errors, despite a line-of-sight link between the ground transmitter and ground receiver. To address this issue at the ground transmitter, the conjugates of a known sequence of complex *LP* mode fields was transmitted toward the UAV and then reflected back to the ground transmitter to determine the optimum angle for pointing the optical beam from the ground transmitter toward the UAV. Adjustments to the pointing angle were made on the ground transmitter using a rotating shaft, translation stages, and goniometers until the exact LP mode was acquired on the reflected optical signal. Similarly, at the ground receiver, beam tracking of the signals was performed to avoid tip-tilt errors using a rotation shaft, translation stages, and goniometers. Using the conjugate of a known *LP* mode, the direction of arrival of the received optical beam was determined for maximizing spatial acquisition. After the optimal angles were determined, the pointing angle and angle of arrivals were fixed, as the UAV travelled in a straight line from the initial point. An alternative method for beam tracking is to measure the displacement offsets of the arriving at the detector, which translate into angles of arrival variations [61].

The SINR threshold $SINR\gamma$ was set at the minimum level for turbulence-free transmission under heavy rain, such that:

$$SINR_\gamma = \frac{\sum\limits_{i=1}^{8} P_i}{\bar{r}_i} \tag{13}$$

where $\sum_{i=1}^{8} P_i$ refers to the sum of the transmitted power in all desired modes and $\bar{r}_i$ is the average receiver noise power per mode. The calculated $SINR\gamma$ value was 25 dB.

As shown in Table 1, two different *LP* modes were used, for the primary channel and backup channels, under the same weather condition. The time-varying primary and backup channels were used for obtaining the composite channel, with the aid of a micro-electromechanical systems (MEMS) optical switch for temporal switching between the two channels. The MEMS switch is controlled dynamically using an algorithm designed LabVIEW software by National Instruments (Austin, TX, USA), for automated switching between the two channels based on the comparison of the current SINR to the threshold SNR value, $SINR\gamma$. While the received SINR of the primary channel is equal to greater than $SINR\gamma$, the received data from the primary channel are forwarded to the composite channel by the MEMS switch. On the other hand, when the received SINR of the primary channel is less than $SINR\gamma$, the received data from the backup channel is forwarded to the composite channel by the MEMS switch.

A key parameter for indicating the strength of the atmospheric turbulence is the refractive index structure parameter, C_n^2, which was evaluated by transmitting the concerned mode and then calculating the scintillation index at the receiver using the intensity profile measurements from a charge-coupled-device camera. The scintillation index is given by the Rytov variance [62]:

$$\sigma^2 \approx \frac{\langle I^2 \rangle - \langle I \rangle^2}{\langle I \rangle^2} \tag{14}$$

where I is the on-axis beam intensity and the angle brackets <> denote the ensemble average. The approach for measuring the scintillation index is similar to that in [61]. The refractive index structure parameter C_n^2 is then evaluated by substituting the scintillation index into:

$$\sigma^2 = 1.23 C_n^2 k^{7/6} L^{11/6} \tag{15}$$

where wave number $k = 2\pi/\lambda$ and L is the link distance. Using Equation (13) to Equation (14), the C_n^2 values were computed for various weather conditions based on the data transmission experiments using the designed FSO transceiver. The turbulence strength and turbulence fluctuation are indicated by C_n^2 and the Rytov variance σ^2, respectively. The values of C_n^2 in the atmosphere are typically in the range from 10^{-17} m$^{-2/3}$ for weaker turbulence strength to 10^{-13} m$^{-2/3}$ for stronger turbulence strength. The value of σ^2 is typically related to the refractive index inhomogeneities C_n^2, optical wavelength λ, and the propagating distance L. A higher value of σ^2 generally represents stronger turbulence fluctuation [62]. Weak turbulence is associated with $\sigma^2 < 1$, and moderate fluctuation conditions are characterized by $\sigma^2 \approx 1$. Strong fluctuations are associated with $\sigma^2 > 1$ [62].

5. Results and Discussion

To evaluate the effectiveness of spatial mode diversity using linearly polarized modes for maintaining the signal quality of a UAV-based free space optical system, the time-varying SINR of the primary, backup, and composite channels were measured under various weather conditions: (i) light rain, (ii) medium rain, (iii) heavy rain, (iv) clear day. The rain level was classified as 'light', 'medium', and 'heavy' for precipitation rates of accumulation of about 0 to 2 mm per h, 2 to 10 mm per h, and 10 to 50 mm per h, respectively [63]. For each weather condition, the minimum and maximum C_n^2 values were computed to determine the range of turbulence strengths.

Although the signals were received at 20 Gbps, the acquisition and evaluation of the channel matrix and interfering modes at high data rates were computationally intensive and required time. Thus, the SINR was sampled at 1 Gbps. In addition, the hovering time of the UAV was 45 min, so a 30 min interval was selected to give the UAV sufficient time to return to the ground station.

For each case, the time-varying SINR is plotted for the primary channel, backup channel, and the composite channel. The composite channel comprises various temporal segments of data from the primary channel and the backup channel such that when the SINR is equal to or more than the threshold value of 25 dB, the received data from the primary channel are forwarded to the composite channel. On the other hand, when the SINR on the primary channel drops below 25 dB, the received data from backup channel are forwarded to the composite channel instead.

Figure 2 shows typical plots of the SINR versus time under light rain. The average SINR was 28.5 dB, with a standard deviation of 5.6 dB. Channel 1 was the primary channel (first graph) and Channel 2 was the backup channel (second graph), utilized when the signal in Channel 1 declined below 25 dB. The third graph in Figure 2 shows that the utilization of Channel 2 as a backup channel successfully prevented the SINR from dropping below 25 dB, especially between 1157 s and 1172 s.
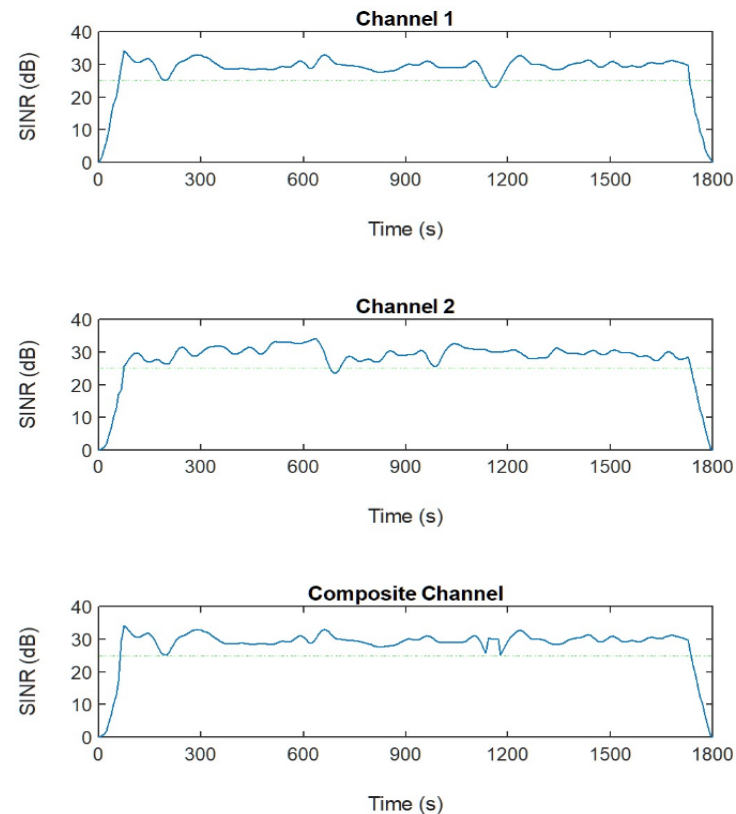

Figure 2. SINR versus time under light rain. Green line shows $SINR\gamma$ value of 25 dB.

Figure 3 shows a typical plot of the SINR versus time under medium rain. The average SINR was 27.5 dB, with a standard deviation of 6.0 dB, underlining deeper variations in the SINR as compared to those under light rain. Channel 3 was the primary channel (first graph) and Channel 4 was the backup channel (second graph), utilized when the SINR in Channel 3 decreased below 25 dB. The third graph in Figure 3 illustrates that employing Channel 4 as a backup channel successfully prevented the composite signal from depreciating below an SINR of 25 dB, preventing link failures to the cloud, especially between 670 s and 701 s, and 1352 s and 1396 s.
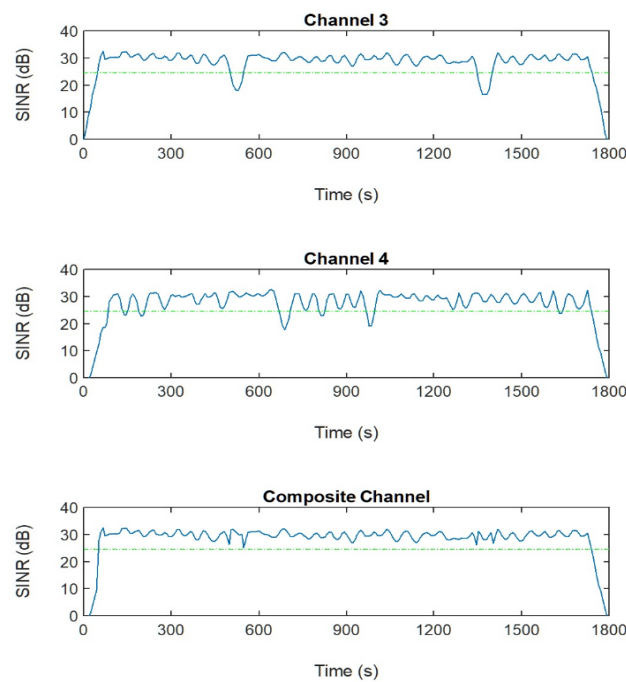
Figure 3. SINR versus time under medium rain. Green line shows *SINRγ* value of 25 dB.

Figure 4 shows typical plots of the SINR versus time under heavy rain. The average SINR was 25.9 dB, with a standard deviation of 6.5 dB, showing more pronounced fluctuations in the SINR as compared to those under medium rain. Channel 7 was the primary channel (first graph) whilst Channel 8 was the backup channel (second graph). The number of regions with compromised SINR in heavy rain was higher than that under medium rain. The SINR for the composite channel, the third plot in Figure 4, shows that leveraging Channel 7 as a backup channel successfully alleviated a large portion of the composite signal from deteriorating below 25 dB, including during a predominant dip between 667 s and 710 s.
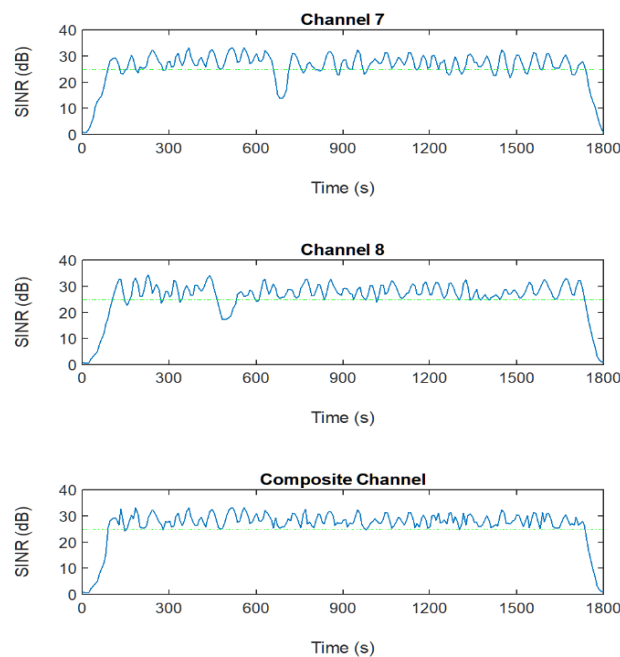

Figure 4. SINR versus time under heavy rain. Green line shows *SINRγ* value of 25 dB.

On a clear day, the average SINR was 30.4 dB. Thus, the backup channel was not required, as the SINR remained above 25 dB, as shown in Figure 5.
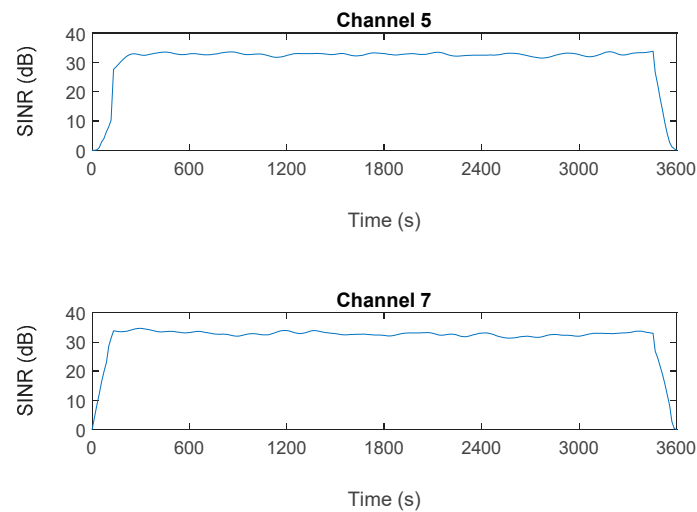

Figure 5. SINR versus time on a clear day.

Uplink and downlink transmissions demonstrated similar SINR characteristics. Overall, a significant improvement in the SINR and outage performance was observed due to spatial mode diversity.

At the receiver, the received optical beam for each channel is demultiplexed to separate spatial modes. It is well-established that refractive index fluctuations in clouds from pressure and temperature fluctuations cause rain [64]. This leads to aberration of the beam wavefront from random power and phase perturbations [65]. This results in the signal initially launched in a particular mode to spread to other modes [66]. The amount of spreading is influenced by the strength of the atmospheric turbulence.

On a clear day, C_n^2 values were found to be between 7×10^{-16} m$^{-2/3}$ and 4×10^{-15} m$^{-2/3}$, peaking in the afternoon. On a clear night, the C_n^2 values were found to be lower, between 8×10^{-17} m$^{-2/3}$ and 1×10^{-16} m$^{-2/3}$. For light rain, the C_n^2 values were in the range of 4×10^{-16} m$^{-2/3}$ to 7×10^{-16} m$^{-2/3}$. For moderate rain, the C_n^2 values were slightly higher, in the range of 6×10^{-16} m$^{-2/3}$ to 9×10^{-16} m$^{-2/3}$, and for heavy rain, the C_n^2 values were higher, in the range of 8×10^{-16} m$^{-2/3}$ to 2×10^{-15} m$^{-2/3}$. The C_n^2 values were found to vary more on a clear day than during rainfall.

The power coupling coefficients were computed for all channels using a noninterferometric modal decomposition method [53], under various weather conditions, at the minimum and maximum C_n^2 values. With knowledge of the power coupling coefficients, the modal crosstalk matrices were constructed, without and with spatial mode diversity. The power coupling coefficients were normalized to the total received optical power for the set of modes present.

Samples of inter-modal crosstalk matrices before mode diversity are shown in Figures 6 and 7, at the minimum and maximum C_n^2 values, respectively. Samples of inter-modal crosstalk matrices after mode diversity are shown in Figures 8 and 9. For clear weather conditions in the day and at night, the power in the dominant mode was more than 75%. Under rain, power from the transmitted mode leaked into adjacent modes. The heavier the rain, the more substantial the spreading of power into adjacent modes due to increased atmospheric turbulence.

Under light rain, the power in the dominant mode was in the range of 68% to 75% before channel diversity reception and 79% to 83% after mode diversity and power were successfully maintained in the dominant modes through the switch to the backup channels during SINR dips. Under medium rain, the power in the dominant mode was in the range of 64% to 68% prior to mode diversity and improved to 75% to 78% in the presence of mode

diversity. Under heavy rain, the power in the dominant mode was approximately 56% to 63% without mode diversity reception and increased to 71% to 75% with mode diversity reception. Uplink and downlink data transmissions demonstrated similar power coupling coefficient characteristics, whereas uplink and downlink data transmissions demonstrated similar power coupling coefficient characteristics.
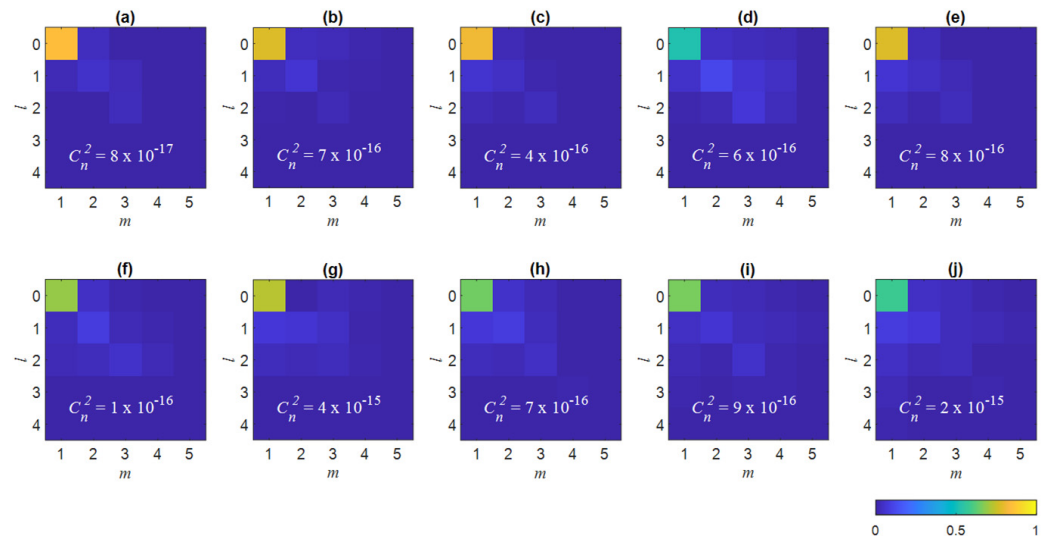

Figure 6. Variation in normalized power coupling coefficients for on *LP 01* mode before spatial mode diversity: (**a**,**f**) clear night, (**b**,**g**) clear day, (**c**,**h**) light rain, (**d**,**i**) medium rain, (**e**,**j**) heavy rain. Top panel (**a**–**e**) shows the power coupling coefficients at low-refractive-index structure values, and bottom panel shows (**f**–**j**) those at high-refractive-index structure values. Color legend of normalized power coupling coefficients for all plots is on the bottom right corner.
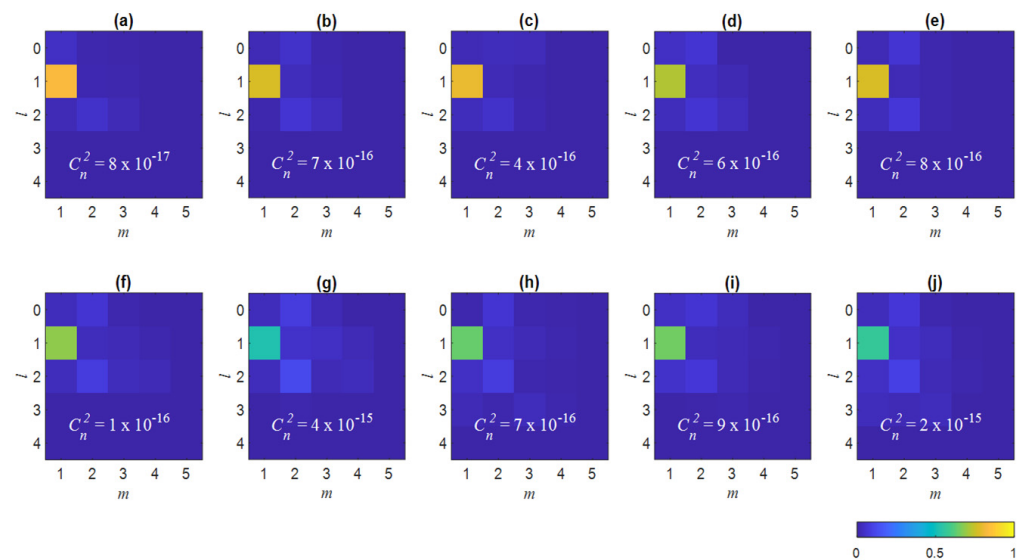

Figure 7. Variation in normalized power coupling coefficients on *LP11* mode before spatial mode diversity: (**a**,**f**) clear night, (**b**,**g**) clear day, (**c**,**h**) light rain, (**d**,**i**) medium rain, (**e**,**j**) heavy rain. Top panel (**a**–**e**) shows the power coupling coefficients at low-refractive-index structure values, and bottom panel shows (**f**–**j**) those at high-refractive-index structure values. Color legend of normalized power coupling coefficients for all plots is on the bottom right corner.
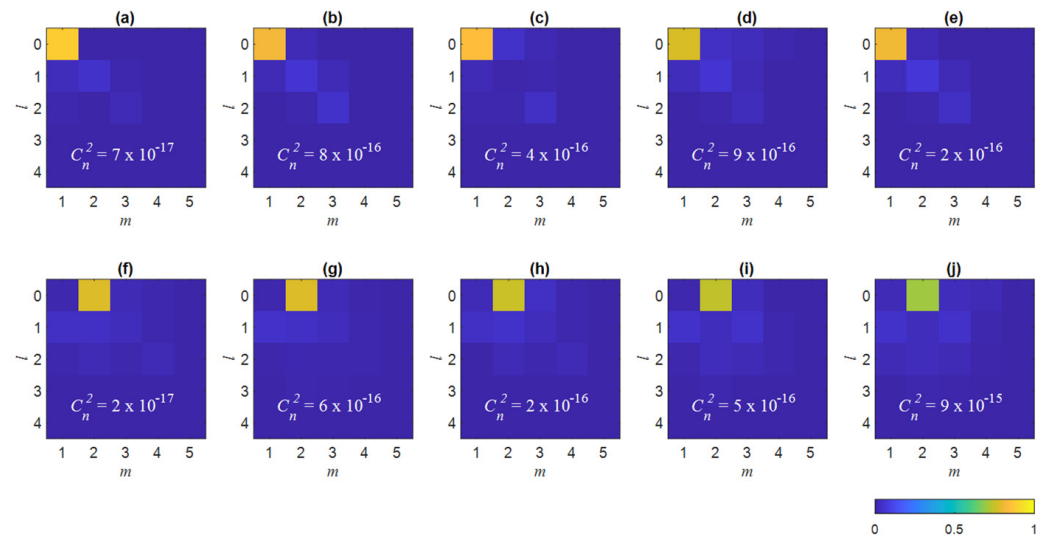
Figure 8. Variation in normalized power coupling coefficients on *LP01* mode after spatial mode diversity reception: (**a**,**f**) clear night, (**b**,**g**) clear day, (**c**,**h**) light rain, (**d**,**i**) medium rain, (**e**,**j**) heavy rain. Top panel (**a**–**e**) shows the power coupling coefficients for primary channel at low-refractive-index structure values, and the bottom panel shows (**f**–**j**) those for backup channel at high-refractive-index structure values. Color legend of normalized power coupling coefficients for all plots is on the bottom right corner.
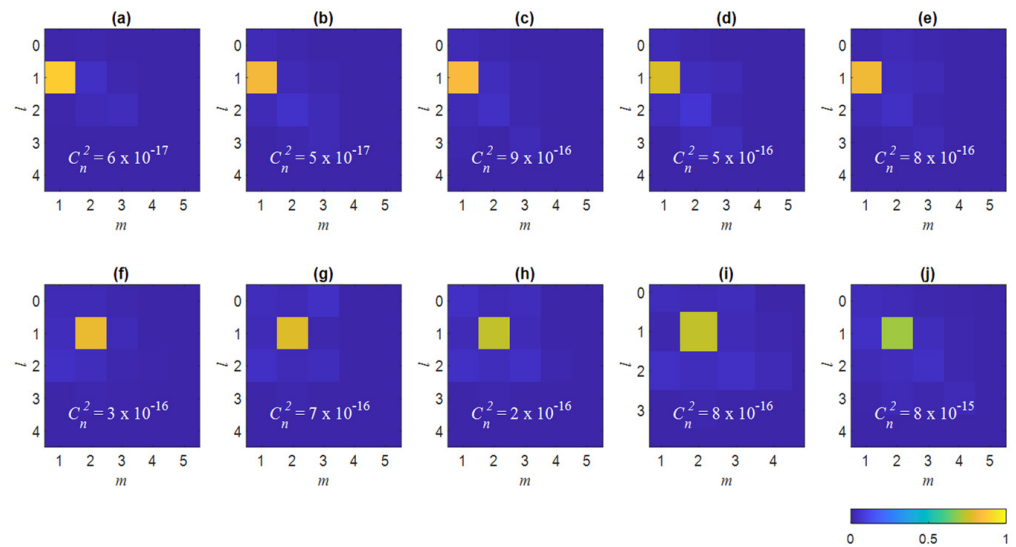

Figure 9. Variation in normalized power coupling coefficients on *LP11* mode after spatial mode diversity: (**a**,**f**) clear night, (**b**,**g**) clear day, (**c**,**h**) light rain, (**d**,**i**) medium rain, (**e**,**j**) heavy rain. Top panel (**a**–**e**) shows the power coupling coefficients for primary channel at low-refractive-index structure values, and the bottom panel shows (**f**–**j**) those for backup channel at high-refractive-index structure values. Color legend of normalized power coupling coefficients for all plots is on the bottom right corner.

Overall, 25% to 44% of power was leaked to other modes during rainfall, prior to mode diversity. The power leakage was more significant for adjacent modes to the dominant modes and gradually decreased for modes further away from the dominant modes. With increased turbulence strength, the crosstalk was more prevalent and the power distribution of the modes was more dispersed. After mode diversity reception, an increase of 10% to 19% in the dominant mode power was observed. A larger amount of power was successfully

maintained in the dominant modes through the switch to the backup channels during SINR dips.

The inter-modal crosstalk matrices for the primary channel, secondary channel, and composite channel after mode diversity is shown Figure 10. The power in the dominant mode of each channel was improved under all weather conditions. Without the mode diversity scheme, there were interruptions in the data transmission from sensors. By incorporating mode diversity, uninterrupted data transmission from sensors was observed, even under heavy rain due to the backup channels on different LG modes experiencing different channel degradations from the primary channels.
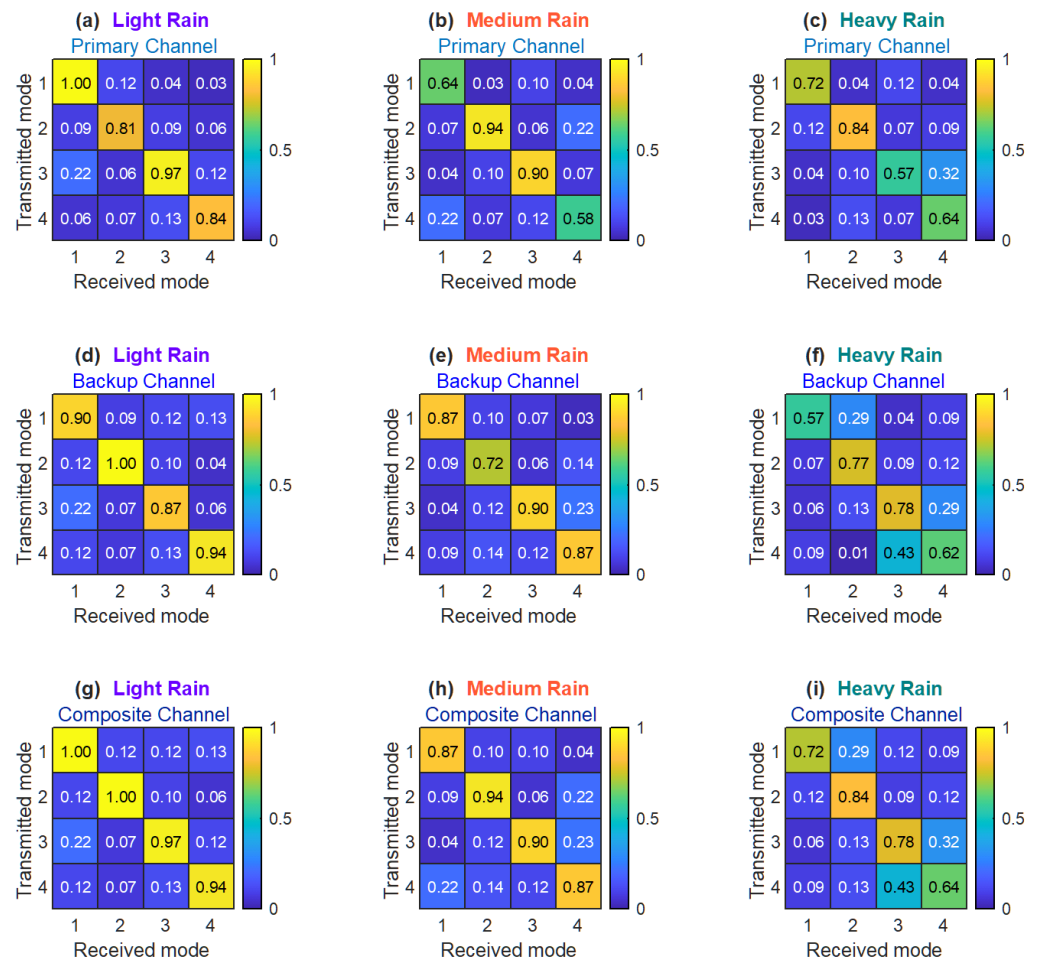

Figure 10. Inter-modal crosstalk matrices for primary channel and secondary channel before mode diversity, and composite channel after mode diversity. The transmitted mode number and received mode number, i, are given in Table 1. The color legend shows the normalized power coupling coefficient.

The average diversity gain from spatial mode diversity was 0.97 dB. The average bit error rate (BER) versus SINR for all channels under various weather conditions was measured and compared, without and with spatial mode diversity, as shown in Figure 11. It was observed that spatial mode diversity successfully enhanced the BER by 38% to 55% from the original BER. After spatial mode diversity, a satisfactory BER below the 7% forward error correction (FEC) limit of 3.8×10^{-3} was attained, at SINRs higher than 20 dB, under all levels of rain. An FEC of 7% was used to provide a 0.3 dB coding gain to better mitigate atmospheric turbulence.
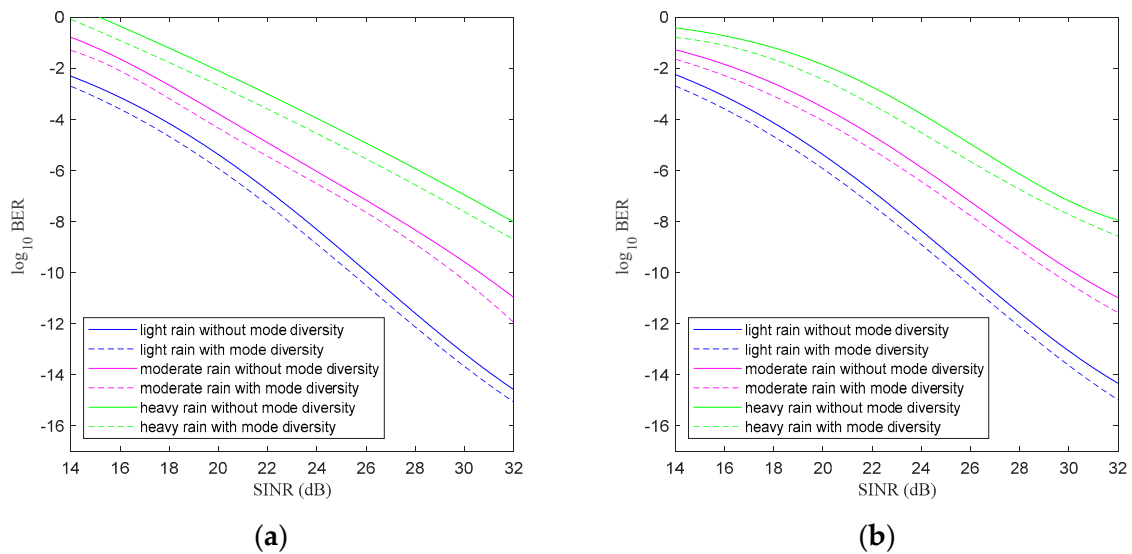
Figure 11. BER for all channels under varying rain levels. (**a**) Composite Channel 1,2. (**b**) Composite Channels 3,4.

Through UAV-FSO spatial diversity, despite mobility restrictions due to floods, vital health statistics from injured flood victims could be forwarded to a patient cloud-based health monitoring system accurately and timely, for hospitals to make critical preparations for relevant medical treatment upon the victims' arrival.

To verify the experimental measurements, the average values of C_n^2 were computed using [67]:

$$
\begin{aligned}
C_n^2 = {} & 3.8 \times 10^{-14} w + 2.0 \times 10^{-15} T - 2.8 \times 10^{-15} W \\
& + 2.9 \times 10^{-17} W^2 - 1.1 \times 10^{-19} W^3 - 2.5 \times 10^{-15} S \\
& + 1.2 \times 10^{-15} S^2 - 8.5 \times 10^{-17} S^3 - 5.3 \times 10^{-13}
\end{aligned}
\tag{16}
$$

where T is the average air temperature, W is the average relative humidity, S is the average wind speed from the local weather station, and w is a scaling coefficient. The average values of C_n^2 using [67] were 3×10^{-15} on a clear day, 1×10^{-16} on a clear night, 6×10^{-16} under light rain, 8×10^{-16} under moderate rain, and 2×10^{-15} under heavy rain. This concurred with earlier experimental values computed using the scintillation index within 1×10^{-15}. The refractive index structure parameter C_n^2 was in the range of 1×10^{-15} to 1×10^{-13}. Based on the turbulence strength classification in [62], this indicated weak to moderat turbulence.

A probability distribution function of the C_n^2 values from the experiment could be computed to determine if this adhered to relevant channel probability distribution functions for FSO spatial mode diversity and FSO aerial communications such as Malaga, log normal, Gamma-Gamma, Nagakami, and others [68–72]. Log normal and Gamma-Gamma channel models are considered as special cases of the Malaga channel model, for weak turbulence and moderate-strong turbulence, respectively [72].

Nevertheless, comparison of the time-varying SINR plots from the experiment with existing channel models do not provide accurate time-varying error analysis, as existing channel models are probabilistic [73]. Existing channel models only provide the statistical averages for the random variations and do not describe the evolution of the channel characteristics with time. In simulations modelling the FSO channel, the time-varying atmospheric turbulence is typically emulated by continuously upgrading the random phase patterns to model random irradiance fluctuations, based on a known channel probability distribution function. This is only valid when the atmospheric turbulence is stationery during the laser pulse width [74]. Expanding on the previous work, we performed the false-nearest-neighbors algorithm on the measured time-varying channel matrix, which revealed that the fraction of false nearest neighbors converged to 0. This indicated the

presence of nonlinear deterministic chaos. This opens up new possibilities for research on state-space reconstruction and the dynamic attractor for modeling the nonlinear FSO-UAV channel matrix.

6. Conclusions

A 4 × 2-channel UAV-based spatial mode diversity FSO system was developed for post-flood recovery communications, achieving 2.4 Mbps for a distance of 400 m, under various weather conditions. Spatial mode diversity was realized by using distinct linearly polarized spatial modes in the primary and backup channels. Backup channels were used when the SINR in the primary channels declined below 25 dB. SINR plots from the composite channel showed that dips in the SINR from atmospheric fluctuations were successfully mitigated through spatial mode diversity. The power in the dominant modes increased by 10% to 19% through temporal switching to backup channels during SINR dips in the primary channels. Hence, this provided uninterrupted transmission, even under heavy rain. The spatial mode diversity scheme improved the BER by 38% to 55% compared to the original BER. In the future, the number of modes used for spatial mode diversity may be extended in conjunction with the maximal-ratio combination for better signal quality. The UAV-based spatial mode diversity FSO system is valuable for rapid recovery communications after natural disasters, especially when conventional ground base stations are damaged. Further analysis of nonlinear time-varying deterministic channel characteristics would be valuable for emulating atmospheric turbulence under various weather conditions, toward the implementation of more efficient turbulence compensation approaches.

References

1. Tabari, H. Climate change impact on flood and extreme precipitation increases with water availability. *Sci. Rep.* **2020**, *10*, 13768. [CrossRef]
2. Veettil, P.C.; Raghu, P.T.; Ashok, A. Information quality, adoption of climate-smart varieties and their economic impact in flood-risk areas. *Environ. Dev. Econ.* **2020**, *26*, 45–68. [CrossRef]
3. Kundzewicz, Z.W.; Su, B.; Wang, Y.; Wang, G.; Wang, G.; Huang, J.; Jiang, T. Flood risk in a range of spatial perspectives—From global to local scales. *Nat. Hazards Earth Syst. Sci.* **2019**, *19*, 1319–1328. [CrossRef]
4. Baharuddin, K.A.; Wahab, S.F.A.; Ab Rahman, N.H.N.; Mohamad, N.A.N.; Kamauzaman, T.H.T.; Noh, A.Y.M.; Majod, M.R.A. The record-setting flood of 2014 in Kelantan: Challenges and recommendations from an emergency medicine perspective and why the medical campus stood dry. *Malays. J. Med. Sci.* **2015**, *22*, 1–7.
5. Reuters. Malaysia Floods Hit Seven States Forcing Thousands to Evacuate. 2022. Available online: https://edition.cnn.com/2022/01/02/asia/malaysia-floods-evacuation-intl-hnk/index.html (accessed on 23 April 2022).
6. Hassan, H. Peninsular Malaysia hit by '1-in-100-year' rainfall, government says amid severe flooding. *The Straits Time*, 20 December 2021.
7. Malaysia National Disaster Management Agency (NADMA). Malaysia-Floods and Landslides, Update. In European Union Civil Protection and Humanitarian Aid (ECHO) Daily Flash, European Civil Protection and Humanitarian Aid. 3 January 2022. Available online: https://reliefweb.int/report/malaysia/malaysia-floods-and-landslides-update-nadma-met-malaysia-media-echo-daily-flash-3 (accessed on 23 April 2022).
8. Chen, G. Floods: 472 areas in Petaling, KL and Hulu Langat hit by water cuts as treatment plants shut down. *The Star*, 19 December 2021.

9.   TNB shuts down 333 power substations in six states hit by floods. *Malay Mail*, 19 December 2021.

10. Over 100 Celcom 2G/4G Network Sites impacted by Flood, Restoration in Progress. *Malaysian Wireless*, 23 December 2021.

11. MCMC: 276 Communication Tower Still Down, PJ Among Highest. *Business Today*, 25 December 2021.

12. Hu, J.; Huang, H.; Yang, L.; Zhu, Y. A multi-objective optimization framework of constellation design for emergency observation. *Adv. Space Res.* **2020**, *67*, 531–545. [CrossRef]

13. Wang, X.; Zhang, H.; Bai, S.; Yue, Y. Design of agile satellite constellation based on hybrid-resampling particle swarm optimization method. *Acta Astronaut.* **2021**, *178*, 595–605. [CrossRef]

14. Liu, Y.; Wan, Z.; Dai, Y.; Zhao, Y.; Liu, Q.; Ji, C. Emergency Constellation Design Based on Micro SAR Satellite. In Proceedings of the 2021 Global Reliability and Prognostics and Health Management, Nanjing, China, 15–17 October 2021; pp. 1–5.

15. Alam, S.; Kurt, G.K.; Yanikomeroglu, H.; Zhu, P.; Dao, N.D. High Altitude Platform Station Based Super Macro Base Station Constellations. *IEEE Commun. Mag.* **2021**, *59*, 103–109. [CrossRef]

16. Alexandre, L.C.; Linhares, A.; Neto, G.; Sodre, A.C. High-Altitude Platform Stations as IMT Base Stations: Connectivity from the Stratosphere. *IEEE Commun. Mag.* **2021**, *59*, 30–35. [CrossRef]

17. Kurt, G.K.; Khoshkholgh, M.G.; Alfattani, S.; Ibrahim, A.; Darwish, T.S.J.; Alam, S.; Yanikomeroglu, H.; Yongacoglu, A. A Vision and Framework for the High Altitude Platform Station (HAPS) Networks of the Future. *IEEE Commun. Surv. Tutorials* **2021**, *23*, 729–779. [CrossRef]

18. Deka, R.; Mishra, V.; Ahmed, I.; Anees, S.; Alam, M.S. Performance Analysis of HAPS Assisted Dual-Hop Hybrid RF/FSO System. In Proceedings of the 2021 IEEE 94th Vehicular Technology Conference (VTC2021-Fall), Virtual, 27–30 September 2021; pp. 1–6.

19. Na, Z.; Wang, Y.; Xiong, M. Joint trajectory and power optimization for NOMA-based high altitude platform relaying system. *Wirel. Net.* **2021**, 1–12. [CrossRef]

20. Ke, M.; Gao, Z.; Huang, Y.; Ding, G.; Ng, D.W.K.; Wu, Q.; Zhang, J. An Edge Computing Paradigm for Massive IoT Connectivity Over High-Altitude Platform Networks. *IEEE Wirel. Commun.* **2021**, *28*, 102–109. [CrossRef]

21. Hu, B.; Wang, L.; Chen, S.; Cui, J.; Chen, L. An Uplink Throughput Optimization Scheme for UAV-Enabled Urban Emergency Communications. *IEEE Internet Things J.* **2021**, *9*, 4291–4302. [CrossRef]

22. Alzahrani, B.; Oubbati, O.S.; Barnawi, A.; Atiquzzaman, M.; Alghazzawi, D. UAV assistance paradigm: State-of-the-art in applications and challenges. *J. Netw. Comput. Appl.* **2020**, *166*, 102706. [CrossRef]

23. Lin, Y.; Wang, T.; Wang, S. Trajectory Planning for Multi-UAV Assisted Wireless Networks in Post-Disaster Scenario. In Proceedings of the 2019 IEEE Global Communications Conference (GLOBECOM), Waikoloa, HI, USA, 9–13 December 2019; pp. 1–6.

24. Arafat, M.Y.; Moh, S. Localization and Clustering Based on Swarm Intelligence in UAV Networks for Emergency Communications. *IEEE Internet Things J.* **2019**, *6*, 8958–8976. [CrossRef]

25. Yang, Z.; Liu, H.; Chen, Y.; Zhu, X.; Ning, Y.; Zhu, W. UEE-RPL: A UAV-Based Energy Efficient Routing for Internet of Things. *IEEE Trans. Green Commun. Netw.* **2021**, *5*, 1333–1344. [CrossRef]

26. Lin, N.; Liu, Y.; Zhao, L.; Wu, D.O.; Wang, Y. An Adaptive UAV Deployment Scheme for Emergency Networking. *IEEE Trans. Wirel. Commun.* **2021**, *21*, 2383–2398. [CrossRef]

27. Dhasarathan, V.; Singh, M.; Malhotra, J. Development of high-speed FSO transmission link for the implementation of 5G and Internet of Things. *Wirel. Net.* **2019**, *26*, 2403–2412. [CrossRef]

28. Chowdhury, M.Z.; Shahjalal, M.; Hasan, M.; Jang, Y.M. The role of optical wireless communication technologies in 5G/6G and IoT solutions: Prospects, directions, and challenges. *Appl. Sci.* **2019**, *9*, 4367. [CrossRef]

29. Wang, F.; Liu, Y.; Jiang, F.; Chi, N. High speed underwater visible light communication system based on LED employing maximum ratio combination with multi-PIN reception. *Opt. Commun.* **2018**, *425*, 106–112. [CrossRef]

30. Alsabah, M.; Naser, M.A.; Mahmmod, B.M.; Abdulhussain, S.H.; Eissa, M.R.; Al-Baidhani, A.; Noordin, N.K.; Sait, S.M.; Al-Utaibi, K.A.; Hashim, F. 6G Wireless Communications Networks: A Comprehensive Survey. *IEEE Access* **2021**, *9*, 148191–148243. [CrossRef]

31. Sun, X.; Yu, L.; Zhang, T. Latency Aware Transmission Scheduling for Steerable Free Space Optics. In *IEEE Transactions on Mobile Computing*; IEEE: Piscataway, NJ, USA, 2021; p. 1. [CrossRef]

32. Wu, D.; Sun, X.; Ansari, N. An FSO-Based Drone Assisted Mobile Access Network for Emergency Communications. *IEEE Trans. Netw. Sci. Eng.* **2019**, *7*, 1597–1606. [CrossRef]

33. Ansari, N.; Wu, D.; Sun, X. FSO as backhaul and energizer for drone-assisted mobile access networks. *ICT Express* **2020**, *6*, 139–144. [CrossRef]

34. Zhang, T.; Sun, X.; Wang, C. On Optimizing the Divergence Angle of an FSO based Fronthaul Link in Drone Assisted Mobile Networks. *IEEE Internet Things J.* **2021**, *9*, 6914–6921. [CrossRef]

35. Swaminathan, R.; Sharma, S.; Vishwakarma, N.; Madhukumar, A.S. HAPS-Based Relaying for Integrated Space–Air–Ground Networks With Hybrid FSO/RF Communication: A Performance Analysis. *IEEE Trans. Aerosp. Electron. Syst.* **2021**, *57*, 1581–1599. [CrossRef]

36. Shah, S.; Siddharth, M.; Vishwakarma, N.; Swaminathan, R.; Madhukumar, A.S. Adaptive-Combining-Based Hybrid FSO/RF Satellite Communication With and Without HAPS. *IEEE Access* **2021**, *9*, 81492–81511. [CrossRef]

37. Trichili, A.; Park, K.H.; Zghal, M.; Ooi, B.S.; Alouini, M.S. Communicating using spatial mode multiplexing: Potentials, challenges, and perspectives. *IEEE Commun. Surv. Tutor.* **2019**, *21*, 3175–3203. [CrossRef]

38. Trichili, A.; Cox, M.A.; Ooi, B.S.; Alouini, M.-S. Roadmap to free space optics. *J. Opt. Soc. Am. B* **2020**, *37*, A184–A201. [CrossRef]

39. Cox, M.A.; Cheng, L.; Rosales-Guzmán, C.; Forbes, A. Modal diversity for robust free-space optical communications. *Phys. Rev. Appl.* **2018**, *10*, 024020. [CrossRef]

40. Li, L.; Song, H.; Zhang, R.; Zhao, Z.; Liu, C.; Pang, K.; Song, H.; Du, J.; Willner, A.N.; Almaiman, A.; et al. Increasing system tolerance to turbulence in a 100-Gbit/s QPSK free-space optical link using both mode and space diversity. *Opt. Commun.* **2020**, *480*, 126488. [CrossRef]

41. Zheng, D.; Li, Y.; Zhou, H.; Bian, Y.; Yang, C.; Li, W.; Qiu, J.; Guo, H.; Hong, X.; Zuo, Y.; et al. Performance enhancement of free-space optical communications under atmospheric turbulence using modes diversity coherent receipt. *Opt. Express* **2018**, *26*, 28879–28890. [CrossRef]

42. Arikawa, M.; Ito, T. Performance of mode diversity reception of a polarization-division-multiplexed signal for free-space optical communication under atmospheric turbulence. *Opt. Express* **2018**, *26*, 28263–28276. [CrossRef]

43. Song, H.; Li, L.; Pang, K.; Zhang, R.; Zou, K.; Zhao, Z.; Du, J.; Song, H.; Liu, C.; Cao, Y.; et al. Demonstration of using two aperture pairs combined with multiple-mode receivers and MIMO signal processing for enhanced tolerance to turbulence and misalignment in a 10 Gbit/s QPSK FSO link. *Opt. Lett.* **2020**, *45*, 3042–3045. [CrossRef]

44. Yousif, B.B.; Elsayed, E.E. Performance Enhancement of an Orbital-Angular-Momentum-Multiplexed Free-Space Optical Link Under Atmospheric Turbulence Effects Using Spatial-Mode Multiplexing and Hybrid Diversity Based on Adaptive MIMO Equalization. *IEEE Access* **2019**, *7*, 84401–84412. [CrossRef]

45. Amphawan, A.; Chaudhary, S.; Neo, T.-K.; Kakavand, M.; Dabbagh, M. Radio-over-free space optical space division multiplexing system using 3-core photonic crystal fiber mode group multiplexers. *Wirel. Netw.* **2020**, *27*, 211–225. [CrossRef]

46. Amphawan, A.; Chaudhary, S.; Ghassemlooy, Z.; Neo, T.-K. 2×2-channel mode-wavelength division multiplexing in Ro-FSO system with PCF mode group demultiplexers and equalizers. *Opt. Commun.* **2020**, *467*, 125539. [CrossRef]

47. Chaudhary, S.; Amphawan, A. Solid core PCF-based mode selector for MDM-Ro-FSO transmission systems. *Photon-Netw. Commun.* **2018**, *36*, 263–271. [CrossRef]

48. Chaudhary, S.; Amphawan, A. Selective excitation of LG 00, LG 01, and LG 02 modes by a solid core PCF based mode selector in MDM-Ro-FSO transmission systems. *Laser Phys.* **2018**, *28*, 075106. [CrossRef]

49. Goodman, J.W. *Introduction to Fourier Optics*; Macmillan Learning: New York, NY, USA, 2017.

50. Chaudhary, S.; Amphawan, A. High-speed MDM-Ro-FSO system by incorporating spiral-phased Hermite Gaussian modes. *Photon-Netw. Commun.* **2018**, *35*, 374–380. [CrossRef]

51. Snyder, A.W.; Love, J.D. *Optical Waveguide Theory (Science Paperbacks)*; Chapman and Hall: London, UK, 1983.

52. Amhoud, E.-M.; Ooi, B.S.; Alouini, M.-S. A Unified Statistical Model for Atmospheric Turbulence-Induced Fading in Orbital Angular Momentum Multiplexed FSO Systems. *IEEE Trans. Wirel. Commun.* **2019**, *19*, 888–900. [CrossRef]

53. Amphawan, A.; O'Brien, D. Modal decomposition of output field for holographic mode field generation in a multimode fiber channel. In Proceedings of the International Conference on Photonics, Langkawi, Malaysia, 5–7 July 2010; pp. 1–5.

54. Rogel-Salazar, J.; Treviño, J.P.; Chávez-Cerda, S. Engineering structured light with optical vortices. *J. Opt. Soc. Am. B* **2014**, *31*, A46–A50. [CrossRef]

55. Amphawan, A.; Payne, F.; O'Brien, D.; Shah, N. Derivation of an analytical expression for the power coupling coefficient for offset launch into multimode fiber. *J. Lightwave Technol.* **2009**, *28*, 861–869. [CrossRef]

56. Andrews, L.C.; Phillips, R.L. *Laser Beam Propagation through Random Media*; SPIE Optical Engineering Press: Bellingham, WA, USA, 1998; pp. 47–50.

57. Ren, Y.; Huang, H.; Xie, G.; Ahmed, N.; Yan, Y.; Erkmen, B.I.; Chandrasekaran, N.; Lavery, M.; Steinhoff, N.K.; Tur, M.; et al. Atmospheric turbulence effects on the performance of a free space optical link employing orbital angular momentum multiplexing. *Opt. Lett.* **2013**, *38*, 4062–4065. [CrossRef] [PubMed]

58. Andrews, L.C. An Analytical Model for the Refractive Index Power Spectrum and Its Application to Optical Scintillations in the Atmosphere. *J. Mod. Opt.* **1992**, *39*, 1849–1853. [CrossRef]

59. Funes, G.; Vial, M.; Anguita, J.A. Orbital-angular-momentum crosstalk and temporal fading in a terrestrial laser link sing single-mode fiber coupling. *Opt. Express* **2015**, *23*, 23133–23142. [CrossRef]

60. Anguita, J.A.; Neifeld, M.A.; Vasic, B.V. Modeling channel interference in an orbital angular momentum-multiplexed laser link. In *Free-Space Laser Communications IX*; International Society for Optics and Photonics: San Diego, CA, USA, 2009; Volume 7464, p. 74640U.

61. Amphawan, A.; Mishra, V.; Nisar, K.; Nedniyom, B. Real-time holographic backlighting positioning sensor for enhanced power coupling efficiency into selective launches in multimode fiber. *J. Mod. Opt.* **2012**, *59*, 1745–1752. [CrossRef]

62. Maurer, T.; Driggers, R.G.; Vollmerhausen, R.H.; Friedman, M.H. NVTherm improvements. In *Infrared and Passive Millimeter-Wave Imaging Systems: Design, Analysis, Modeling, and Testing, Orlando, USA*; International Society for Optics and Photonics: Bellingham, WA, USA, 2002; Volume 4719, pp. 15–23.

63. U.M. Office. National Meteorological Library and Archive Fact Sheet 3—Water in the Atmosphere. 2012. Available online: https://www.metoffice.gov.uk/binaries/content/assets/metofficegovuk/pdf/research/library-and-archive/library/publications/factsheets/factsheet_3-water-in-the-atmosphere.pdf (accessed on 23 April 2022).

64. Falkovich, G.; Fouxon, A.; Stepanov, M.G. Acceleration of rain initiation by cloud turbulence. *Nature* **2002**, *419*, 151–154. [CrossRef]

65. Mahalov, A.; McDaniel, A. Long-range propagation through inhomogeneous turbulent atmosphere: Analysis beyond phase screens. *Phys. Scr.* **2018**, *94*, 034003. [CrossRef]

66. Zhao, L.; Liu, H.; Hao, Y.; Sun, H.; Wei, Z. Effects of Atmospheric Turbulence on OAM-POL-FDM Hybrid Multiplexing Communication System. *Appl. Sci.* **2019**, *9*, 5063. [CrossRef]

67. Sadot, D.; Kopeika, N.S. Forecasting optical turbulence strength on the basis of macroscale meteorology and aerosols: Models and validation. *Opt. Eng.* **1992**, *31*, 200–212. [CrossRef]

68. Sarker, N.A.; Badrudduza, A.S.M.; Islam, S.R.; Islam, S.H.; Kundu, M.K.; Ansari, I.S.; Kwak, K.S. On the Intercept Probability and Secure Outage Analysis of Mixed (α–κ–μ)-Shadowed and Málaga Turbulent Models. *IEEE Access* **2021**, *9*, 133849–133860. [CrossRef]

69. Singh, H. Performance analysis of FSO system with spatial diversity using two-point Padé approximation. *Opt. Quantum Electron.* **2021**, *53*, 1–25. [CrossRef]

70. Wenjing, G.; Ziyuan, S.; Yueying, Z.; Lei, Y. Channel Modeling for Ground-to-UAV Free-Space Optical Communication Systems. In Proceedings of the 26th Optoelectronics and Communications Conference, Hong Kong, China, 3–7 July 2021; Optica Publishing Group: Washington, DC, USA, 2021; p. S4B.6.

71. Khallaf, H.S.; Kato, K.; Mohamed, E.M.; Sait, S.M.; Yanikomeroglu, H.; Uysal, M. Composite Fading Model for Aerial MIMO FSO Links in the Presence of Atmospheric Turbulence and Pointing Errors. *IEEE Wirel. Commun. Lett.* **2021**, *10*, 1295–1299. [CrossRef]

72. El Saghir, B.M.; El Mashade, M.B.; Aboshosha, A.M. Performance analysis of modulating retro-reflector FSO communication systems over Málaga turbulence channels. *Opt. Commun.* **2020**, *474*, 126160. [CrossRef]

73. Cox, M.A.; Mphuthi, N.; Nape, I.; Mashaba, N.; Cheng, L.; Forbes, A. Structured light in turbulence. *IEEE J. Sel. Top. Quantum Electron.* **2020**, *27*, 1–21. [CrossRef]

74. Taylor, G.I. Statistical theory of turbulence-II. *Proc. R. Soc. London. Ser. A Math. Phys. Sci.* **1935**, *151*, 444–454. [CrossRef]